Article

Morphology and Catalytic Performance of MoS$_2$ Hydrothermally Synthesized at Various pH Values

Seung-Jae Lee [1], Yang-Seung Son [2], Jin-Hoon Choi [2,*], Seong-Soo Kim [1] and Sung-Youl Park [1,*]

1 Energy Resources Upcycling Research Laboratory, Korea Institute of Energy Research, 152 Gajeong-ro, Yuseong-gu, Daejeon 34129, Korea; seungjae@kier.re.kr (S.-J.L.); sskim@kier.re.kr (S.-S.K.)
2 Department of Chemical and Biomolecular Engineering, Sogang University, 35 Baekbeom-ro, Mapo-gu, Seoul 04107, Korea; wlwlgeto@naver.com
* Correspondence: choi@sogang.ac.kr (J.-H.C.); redsoil@kier.re.kr (S.-Y.P.); Tel.: +82-2-705-8917 (J.-H.C.); +82-42-860-3046 (S.-Y.P.)

Abstract: Although preparation conditions are known to affect the morphology and catalytic performance of hydrothermally synthesized MoS$_2$, the influence of pH remains unclear. Herein, unsupported MoS$_2$ was prepared from ammonium tetrathiomolybdate (ATTM) by a hydrothermal reaction at various pH values under a reaction pressure of 2 MPa. The physical and chemical properties of the MoS$_2$ samples were characterized, and the catalytic performance for CO methanation was examined. With increasing pH, the morphology of the MoS$_2$ particles transformed from aggregates of irregular grain-like particles to flower-like particles through the agglomeration of fine mesoporous nanoflakes. Hydrothermal synthesis at a pH of 9.5 increased the MoS$_2$ crystallinity by enhancing the stacking of the (0 0 2) lattice plane. The MoS$_2$ samples prepared at pH 7.0 and 9.5 showed increased CO conversion during methanation, which was associated with a low concentration of Mo^{5+} species and the presence of surface sulfate species. Thus, a high pH during catalyst preparation may promote the complete decomposition of ATTM to MoS$_2$ and the formation of sulfur vacancies, which can facilitate methanation.

Keywords: MoS$_2$; hydrothermal reaction; pH; morphology; methanation

1. Introduction

MoS$_2$ is a transition metal dichalcogenide material with a layered structure consisting of stacked S-Mo-S units in the form of a Mo atomic layer interposed between two S layers. The stacked structure of MoS$_2$ can be classified into three polytypes based on symmetry, namely, tetragonal (1T-MoS$_2$), hexagonal (2H-MoS$_2$), and rhombic (3R-MoS$_2$). The S and Mo atoms at the edges of MoS$_2$ crystals are present as anionic and cationic species, respectively, between which strong covalent bonds are formed [1–3]. In addition, the S atoms between the stacked layers of MoS$_2$ are bonded by weak Van der Waals forces, which can be easily broken [1–3]. MoS$_2$ has been applied as a catalyst for various hydrogenation reactions, including hydrodesulfurization [4,5], hydrodenitrogenation [4,6], and methanation [7,8]. Moreover, it has been utilized in hydrogen storage containers [9], manganese and lithium batteries [10–12], and lubricants [13,14]. Recent studies have especially focused on the application of MoS$_2$-based electrodes in beyond-lithium-ion batteries [15,16]. Further, several researchers have thoroughly reviewed the synthesis and structure of MoS$_2$ [2,3] and its applications in fields such as optoelectronics [17,18].

The most commonly used polytype of MoS$_2$ is 2H-MoS$_2$ because it is more stable than 1T-MoS$_2$ and 3R-MoS$_2$. Various morphologies have been reported for 2H-MoS$_2$, including nanorods [19], nanotubes [20], nanoflowers [21], inorganic fullerenes [22], and spherical particles [23,24]. Various methods, such as chemical vapor desorption [25], electrochemical and chemical methods [26], and hydrothermal synthesis [27], have been used to prepare MoS$_2$, and the type of MoS$_2$ structure formed varies depending on the synthesis method. In

particular, the hydrothermal method is known to produce well-crystallized MoS_2 via a simple procedure under moderate operating conditions [27]. Moreover, diverse MoS_2 particle shapes, including nanotubes, nanoflowers, and spherical particles, can be synthesized hydrothermally [28]. The aging time can be tuned, and the amount of ionic liquid added can be varied to yield nanoflower-shaped MoS_2 with high crystallinity and a uniform particle size, which is advantageous for use in lithium batteries or lubricants [28–30]. In addition, porous flower-like microspheres of MoS_2/C that show high electrochemical performance as anode materials for lithium-ion batteries can be synthesized solvothermally [31].

Many researchers have reported the effects of different types of catalyst precursors on the thermal decomposition properties of the products [32–34]. The thermal decomposition of the ammonium heptamolybdate (AHM) precursor with sulfur powder under various sulfidation conditions affected the surface area and catalytic activity during methanation. The optimum S/AHM weight ratio for the as-prepared catalyst was 3:1 [32]. The use of tetra-alkylammonium thiosalts in thermal decomposition resulted in the formation of cheese-like (or sponge-like) MoS_2 [33,34]. The hydrothermal synthesis of ATTM under conditions of high pressure ($\leq$4 MPa) and at a reaction temperature of 350 °C resulted in the improved catalytic performance of MoS_2 during methanation [35]. Although Tian et al. varied the pH of the hydrothermal solution in a narrow range near pH 7.0 to produce amorphous MoS_2 nanospheres [24], the effect of this parameter has not been investigated in detail. Therefore, in this study, MoS_2 was hydrothermally synthesized at a wide range of pH values to investigate the influence of pH on morphology and catalytic performance.

2. Results and Discussion

2.1. Catalyst Morphology

SEM images of the hydrothermally prepared catalysts are shown in Figure 1. The particle sizes of the samples prepared at pH 4.5 and 7.0 ranged between 30 and 50 nm. The catalyst prepared at pH 4.5 consisted of aggregates, in which irregularly shaped particles were interconnected (Figure 1a), whereas the catalyst prepared at pH 7 consisted of particles of varying shapes, instead of agglomerates (Figure 1b). By contrast, the particles prepared at pH 9.5 had a flower-like shape and consisted of petals with a thickness of 10 nm and a length of 100–200 nm that agglomerated to form 300–400 nm microspheres (Figure 1c).

Wei et al. [28] hydrothermally synthesized flower-shaped MoS_2 at 180 °C by adding sodium dithionite ($Na_2S_2O_4$) and thioacetamide (CH_3CSNH_2) to a mixture of ammonia and ammonium molybdate (($NH_4)_6Mo_7O_{24}\cdot 4H_2O$). The authors proposed that the reaction of thioacetamide and hydroxyl ions produced sulfur ions that reduced Mo from Mo^{6+} in the oxide precursor to Mo^{4+} in the sulfide product. Additionally, Sen and Mitra [36] prepared MoS_2 with a flower-like morphology from a solution of ammonium heptamolybdenum and ammonium hydroxide by heating the solution to 60 °C in H_2S gas and hydrothermally treating it at 180 °C in an autoclave. They suggested that the excess hydroxyl ions present in the precursor solution caused the MoS_2 crystallites to grow in a lamellar structure by blocking the (0 0 1) plane of the crystallites. Further, it has been found that a nanoflake morphology can be obtained by thermally decomposing ATTM under H_2 in the presence of elemental sulfur, which might play an important role in suppressing the aggregation of MoS_2 nanoflakes [37]. Consequently, the observation of a flower-like MoS_2 morphology at a high pH was likely due to the presence of excess hydroxyl ions from ammonium hydroxide and abundant sulfur from ATTM [38]. In the hydrothermal reaction system, we suggest that the MoS_2 nanoflakes were created owing to the obstruction of the growth of the (0 0 1) plane by the excess hydroxyl ions. Furthermore, the supply of sulfur during the reaction could induce the self-assembly of the nanoflakes to form flower-like MoS_2 particles.
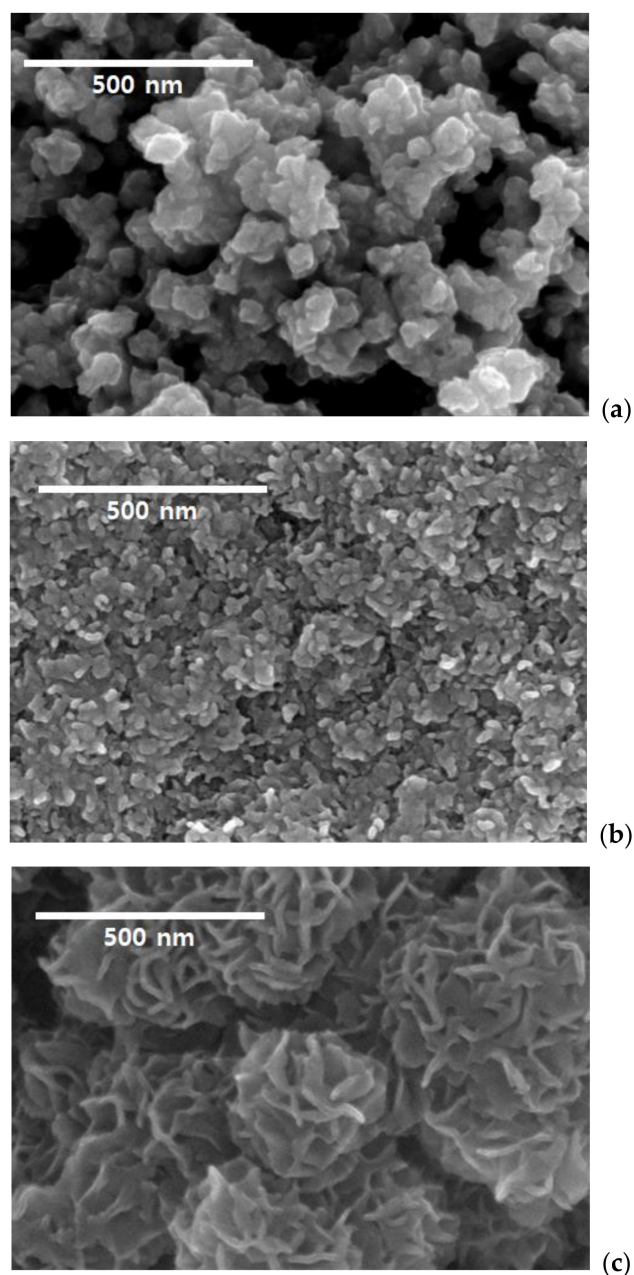
Figure 1. SEM images of MoS$_2$ prepared at (**a**) pH 4.5; (**b**) pH 7.0; and (**c**) pH 9.5.

2.2. Crystalline Structure of Catalysts

A comparison of the XRD patterns of the prepared catalysts with that of commercial MoS$_2$ (Figure 2) confirmed that the samples consisted of the hexagonal phase of MoS$_2$ (JCPDS card No. J87-2416) [39]. However, the diffraction peaks of the prepared MoS$_2$ samples were much broader than those of the commercial sample. As reported by the Chianelli group [40,41], such broad peaks could imply the presence of poorly crystalline MoS$_2$. The strongest diffraction peak at 14° corresponded to the (0 0 2) lattice plane of MoS$_2$ crystallites, whereas the diffraction peaks at 33°, 40°, and 59° were assigned to the (1 0 0), (1 0 3), and (1 1 0) planes, respectively. The XRD patterns of the MoS$_2$ samples prepared at pH 4.5 and 7.0 showed a broad and weak peak corresponding to the (1 0 3) lattice plane, but the (1 0 5) peak was absent. However, for the MoS$_2$ sample prepared at pH 9.5, the peak intensities slightly increased, which indicated that the crystallinity of MoS$_2$ could be enhanced by increasing the pH of the precursor solution to 9.5. Applying the Scherrer equation [41] to the peak at 14°, the average crystallite size of the (0 0 2) lattice plane was

found to increase from 2.7 nm at pH 4.5 to 3.3 nm at pH 9.5 (Table 1). Considering that the d-spacing of the (0 0 2) lattice plane is 6.17 Å [41], the numbers of stacked lattice planes at pH 4.5, 7.0, and 9.5 were calculated to be 4.4, 4.8, and 5.3, respectively.
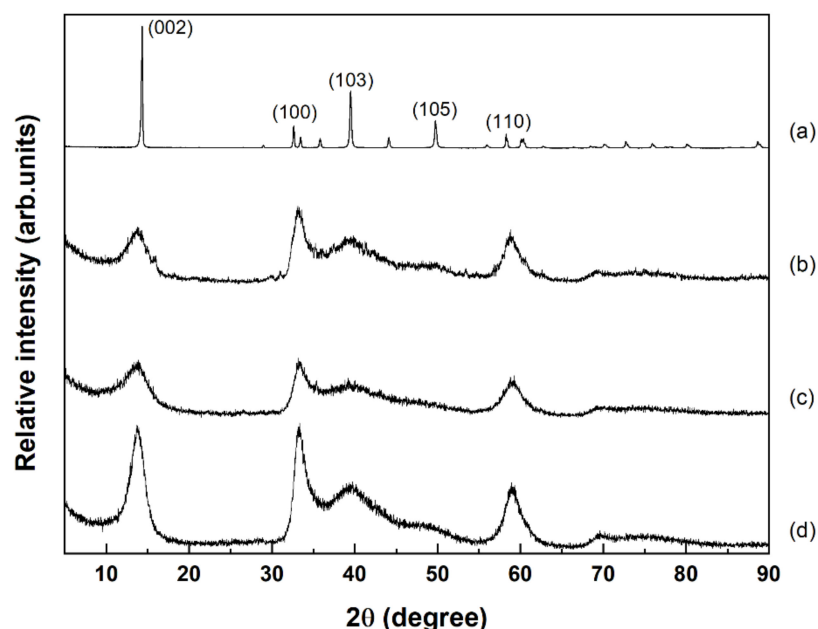

Figure 2. XRD patterns of (**a**) commercial MoS_2 and MoS_2 samples prepared at (**b**) pH 4.5; (**c**) pH 7.0; and (**d**) pH 9.5.

Table 1. Crystalline characteristics of MoS_2 samples.

Catalyst Preparation Conditions		Slab Height (nm)	Number of Stacking Layers
pH	Temperature (°C)		
4.5	350	2.7 ± 0.1	4.4
7.0	350	2.9 ± 0.1	4.8
9.5	350	3.3 ± 0.1	5.3

The HRTEM images (Figure 3) revealed that several MoS_2 layers were stacked to produce a striped pattern along the length of the samples. Moreover, the MoS_2 layers of the samples prepared at pH 9.5 had a higher lateral length than those prepared at pH 4.5 and 7.0. In all the samples, the interlayer distance was observed to be ~0.64 nm (insets, Figure 3), which is similar to that of the (0 0 2) lattice plane in MoS_2 (0.617 nm) [36,42]. Further, the crystallites of MoS_2 prepared at pH 4.5 and 7.0 consisted of 3–5 stacking layers, whereas those prepared at pH 9.5 consisted of 5–9 stacking layers. Considering that the XRD analysis gave mean values, the TEM results were reasonable, and the number of stacking layers in MoS_2 prepared at pH 9.5 likely exceeded those in the samples prepared at pH 4.5 and 7.0.

2.3. Pore Structure of Catalysts

The N_2 adsorption–desorption isotherms of the MoS_2 samples (Figure 4) could be characterized based on the IUPAC classification [43]. MoS_2 prepared at pH 4.5 exhibited a type II isotherm, which could be attributed to the absence of pores or the presence of macropores [43]. In addition, the observation of a type H3 hysteresis loop suggested that the pores were slit shaped and produced by the agglomeration of plate-like particles [39,43]. MoS_2 produced at pH 7.0 exhibited a type IV adsorption isotherm, indicating the existence of mesopores, and showed a type H2 hysteresis loop, suggesting that the pores were ink-bottle-shaped [43]. MoS_2 produced at pH 9.5 showed a type II adsorption isotherm similar to that of the sample produced at pH 4.5. However, the hysteresis loop could be

classified as type H4 [43]. Consequently, although these pores are also slit shaped, their interiors are narrow and uniform. The predicted pore structures were consistent with the SEM observations.
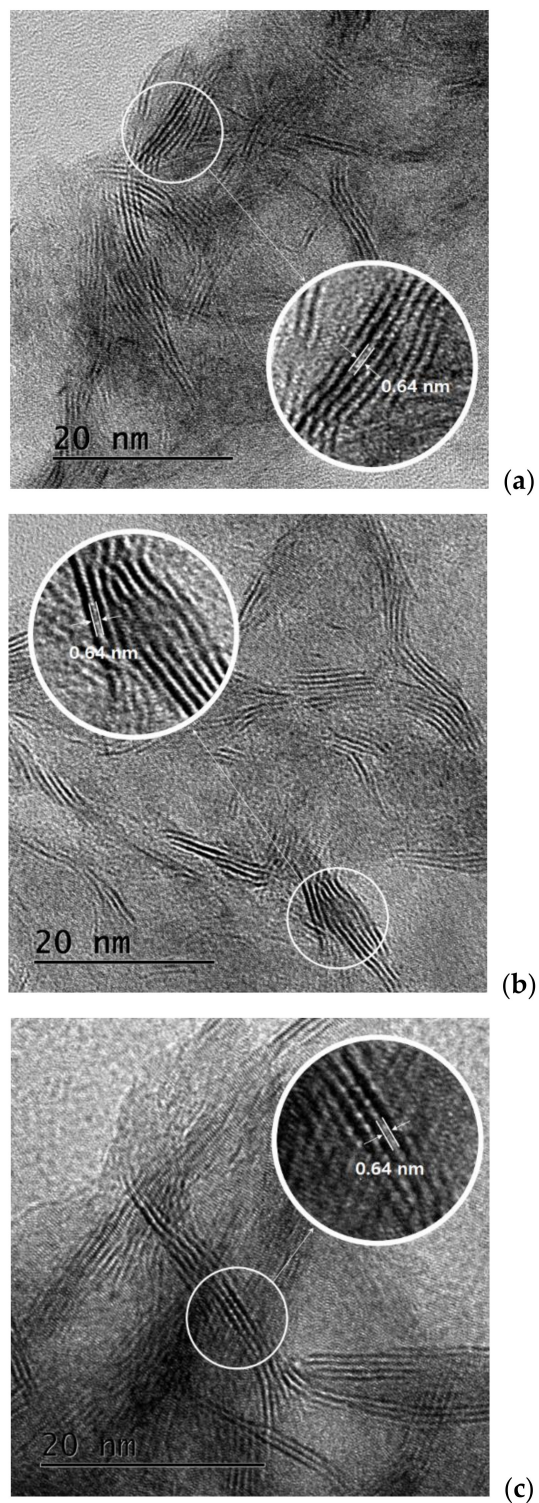

Figure 3. HRTEM images of MoS_2 prepared at (**a**) pH 4.5; (**b**) pH 7.0; and (**c**) pH 9.5.
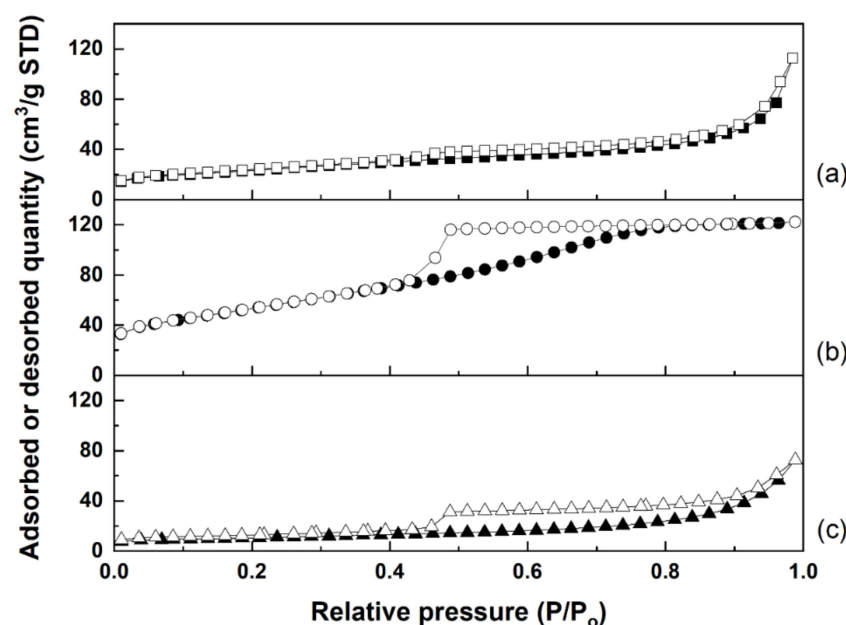
Figure 4. Nitrogen adsorption–desorption isotherms of MoS$_2$ samples prepared at (**a**) pH 4.5; (**b**) pH 7.0; and (**c**) pH 9.5 (The open and filled symbols denote adsorption and desorption, respectively).

The pore properties of the prepared MoS$_2$ samples are summarized in Table 2. The Brunauer–Emmett–Teller (BET) surface area of the MoS$_2$ sample increased from 83.21 to 167.00 m^2/g as the pH of the precursor solution increased from 4.5 to 7.0. This increase was probably due to the creation of mesopores from macropores by the interconnection of the particles, as suggested by the observed changes in morphology. However, further increasing the pH from 7.0 to 9.5 slightly lowered the BET surface area from 167.00 to 158.38 m^2/g, which might be caused by the destruction of micropores to form larger pores during the production of the flower-like particles.

Table 2. Pore properties of MoS$_2$ samples.

Catalyst Preparation Conditions		BET Surface Area (m^2/g)	Average Pore Volume (cm^3/g)	Average Pore Size (nm)
pH	Temperature (°C)			
4.5	350	83.21	0.17	8.39
7.0	350	167.00	0.13	3.42
9.5	350	158.38	0.36	6.15

2.4. Surface Composition of Catalysts

The surface composition of the MoS$_2$ samples was evaluated using XPS. Figures 5 and 6 display the Mo 3d and S 2p XPS spectra, respectively, with the corresponding deconvoluted Lorentzian–Gaussian peaks obtained by the Shirley baseline correction method. In general, Mo 3d peaks consist of Mo 3d$_{5/2}$ and Mo 3d$_{3/2}$ states with a peak area ratio of 3:2 and a separation energy of ~3.1 eV [44]. The Mo 3d$_{5/2}$ binding energies are known to be 228.2–230.1 eV for Mo^{2+} [44,45], 228.7 eV for Mo^{3+} [44], 229.1–230.1 eV for Mo^{4+} [44], 230.9–231.8 eV for Mo^{5+} [44,45], and 231.6–232.7 eV for Mo^{6+} [44]. Moreover, the peak at a binding energy of 226.4 eV can be assigned as S 2S. As shown in Figure 5, most Mo in the prepared MoS$_2$ samples is present as Mo^{4+} in the form of MoS$_2$, as indicated by the strong peaks at binding energies of 229.0 and 232.2 eV, with some Mo^{6+} in the form of MoS$_3$ and MoO$_3$, as indicated by the peaks at 231.4 and 232.1 eV. Wang et al. [44] reported that MoS$_3$ can be produced from ATTM during the MoS$_2$ preparation process by vacuum annealing at 450 °C and that some MoS$_3$ may be oxidized to MoO$_3$ when exposed to air.

The peak at a binding energy of 230.3 eV can be attributed to Mo^{5+} in the form of Mo_2S_5. Based on the results of a TG/DTA analysis, it has been suggested that intermediates such as Mo_2S_5 could form during the phase transformation of MoS_3 into MoS_2 [44]. Thus, the Mo^{5+} could be formed by the incomplete hydrothermal decomposition of ATTM into MoS_2.
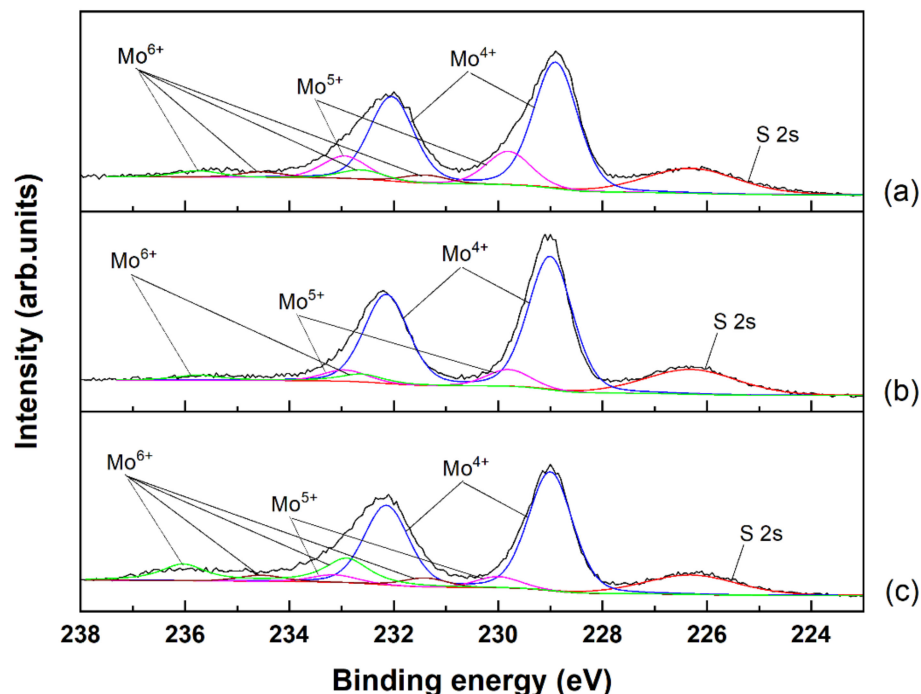
Figure 5. Mo 3d XPS spectra of MoS_2 samples prepared at (**a**) pH 4.5; (**b**) pH 7.0; and (**c**) pH 9.5.
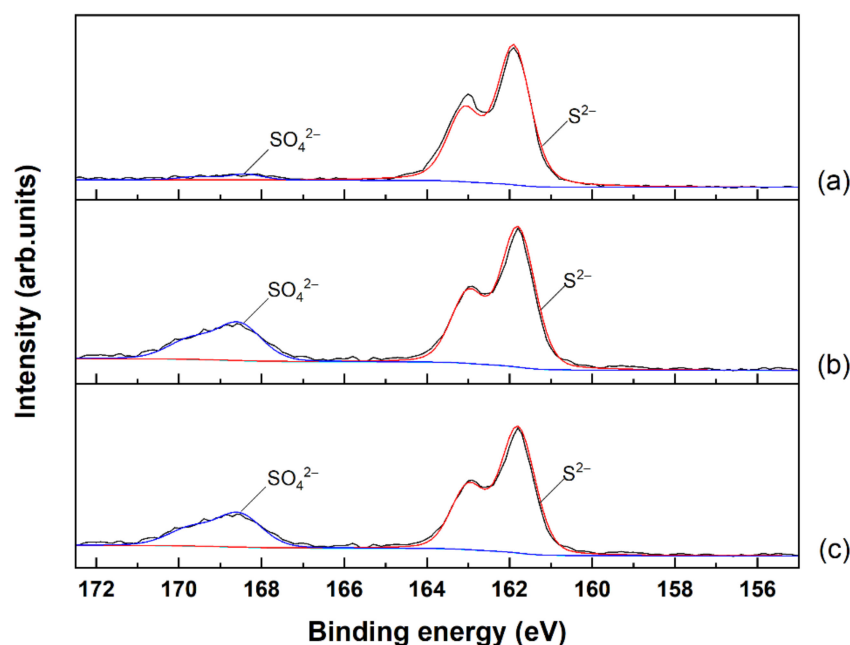
Figure 6. S 2p XPS spectra of MoS_2 samples prepared at (**a**) pH 4.5; (**b**) pH 7.0; and (**c**) pH 9.5.

Typical S 2p peaks consist of S 2p3/2 and S 2p1/2 states with a peak area ratio of 2:1 and a separation energy of ~1.2 eV [44]. As shown in Figure 6, the main S 2p3/2 and S 2p1/2 peaks appear at binding energies of 161.9 and 163.0 eV, respectively, which probably correspond to S^{2-} in MoS_2. The minor peaks observed at 168.9 and 169.9 eV could be associated with sulfate species created by surface oxidation in air [35]. In a previous work,

wherein MoS_2 was hydrothermally prepared at 350 °C in 2 MPa without pH adjustment, it was found that the presence of H_2 in the preparation may deplete the surface sulfur of MoS_3 and Mo_2S_5 to create surface vacancies, which might produce surface sulfates upon exposure to the atmosphere [35]. It is worth noting that the peak areas of the minor peaks increased slightly as the pH values used for MoS_2 preparation increased. Thus, it was postulated that the sulfate species were produced by the oxidation of H_2S adsorbed on the sample prepared at pH 9.5, which might cause the creation of sulfur vacancies on the catalyst surface.

2.5. Catalytic Methanation

The catalytic activities of the prepared MoS_2 samples were evaluated based on CO conversion during methanation (Figure 7). The CO conversion over MoS_2 prepared at pH 4.5 was lower than 3% for reaction times up to 7 h. The poor catalytic activity of this sample was probably due to its low BET surface area and large amount of surface Mo^{5+} species in the form of Mo_2S_5 owing to the incomplete decomposition of ATTM. A previous study found that sulfur in Mo_2S_5 may react with H_2 to form H_2S during methanation at 400 °C in 3 MPa [35]. Thus, during the catalytic reaction, H_2 could be consumed in the reduction of Mo_2S_5 rather than in the methanation of CO. Furthermore, the presence of sulfate species on the MoS_2 surface can be related to sulfur vacancies that can facilitate catalytic reactions [46,47]. The low concentration of sulfate species in the catalyst prepared at pH 4.5 suggested that the creation of sulfur vacancies was suppressed by the low pH value.
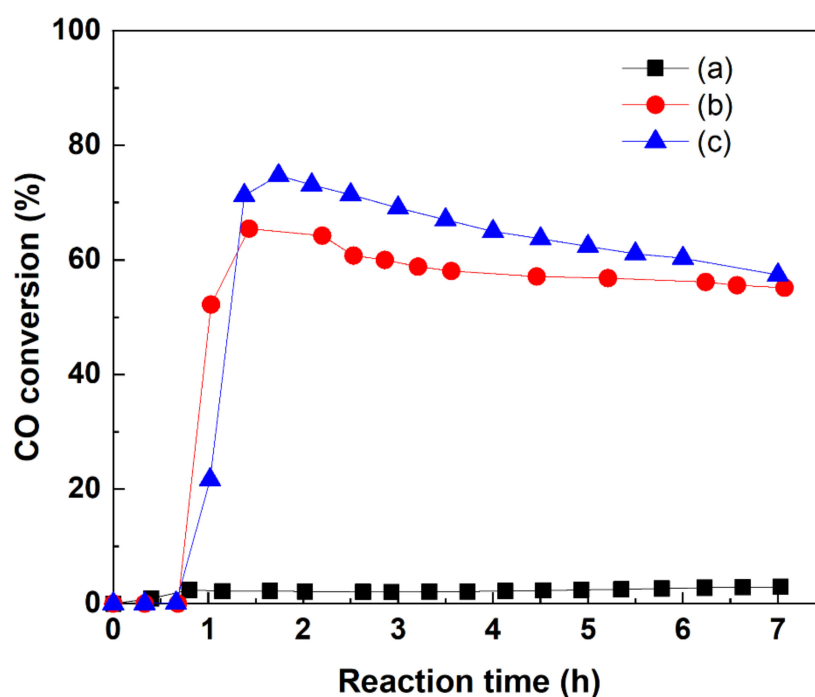

Figure 7. CO conversion over MoS_2 samples prepared at (**a**) pH 4.5; (**b**) pH 7.0; and (**c**) pH 9.5.

With the samples prepared at pH 7.0 and 9.5, the maximum CO conversions were reached within 120 min. At longer reaction times, the CO conversion decreased monotonically. No CO conversion was observed at reaction times shorter than 40 min, likely owing to the aforementioned consumption of H_2 by Mo_2S_5. In general, CO conversion over the sample prepared at pH 9.5 was higher than that over the sample prepared at pH 7.0, with maximum CO conversions of ~75% and 65%, respectively. Although the sample prepared at pH 9.5 had a slightly lower BET surface area than the sample prepared at pH 7.0, the former exhibited a higher CO conversion, which might be induced by the presence of more sulfur vacancies, as evidenced by the sulfate species observed in the XPS spectra. The observed surface sulfate would be initially converted to the vacancies by the reactants

of H_2 and CO during the methanation reaction. In general, such surface vacancies could improve the catalytic activity of MoS_2 [32,48,49]. Furthermore, it has been proposed that active sites such as sulfur vacancies could exist on the curvature of the basal planes of MoS_2, as well as on the edge planes [50,51]. Hence, the samples with a flower-like MoS_2 morphology (prepared at higher pH) might include more surface vacancies of MoS_2 than those with a simple morphology (prepared at lower pH).

## 3. Materials and Methods

3.1. Catalyst Synthesis

MoS_2 catalysts were prepared using a hydrothermal method by varying the pH value of the precursor solution. First, 5 g of ammonium tetrathiomolybdate (ATTM, $(NH_4)_2MoS_4$; Alfa Aesar, 99.99%) as a precursor of MoS_2 was added to 250 mL of deionized water. Then, the pH of the mixture was adjusted to 4.5, 7.0, or 9.5 by adding 0.1 M HCl or 0.1 M NH_4OH. Once the pH was stable, the mixture was transferred to a hydrothermal reactor and then agitated under Ar gas (80 mL/min) for 30 min and H_2 gas (30 mL/min) for 1 h at ambient temperature and pressure. The reactor was pressurized to 2 MPa using a back-pressure regulator. The temperature of the reactor was maintained at 350 °C for 2 h under an atmosphere of H_2 gas (30 mL/min). After the hydrothermal reaction, the pressure and temperature of the reactor were decreased to ambient conditions under Ar gas (200 mL/min) for 12 h. The obtained samples were washed several times with deionized water and acetone, centrifuged at 15,000 rpm for 10 min, and dried in air.

3.2. Catalyst Characterization

The morphologies of the prepared samples were analyzed using scanning electron microscopy (SEM; Hitachi S-4800) and high-resolution transmission electron microscopy (HRTEM; JEOL JEM-2010). To examine the crystalline structures of the samples, X-ray diffraction (XRD) patterns were collected using a Rigaku D/Max-2500 diffractometer equipped with a Cu Kα radiation source (λ = 1.5414 Å) operated at 40 kV and 100 mA. The scanning rate was 2°/min in the 2θ range of 5–90°. The crystalline structure was identified using the Joint Committee on Powder Diffraction Standards (JCPDS) library. To investigate the oxidation states of Mo and S on the sample surface, X-ray photoelectron spectroscopy (XPS) was performed using an Axis Nova spectrometer (Kratos) with a monochromatic Al K_α X-ray source (1486.6 eV) operated at 15 kV and 10 mA under a chamber pressure of 10^{-8} Torr. All binding energies were referenced to that of O 1s (531.0 eV). The baseline corrections for peak fitting were performed using the Shirley method. N_2 adsorption–desorption isotherms of the samples were obtained at 77 K using an ASAP 2020 instrument (Micromeritics Instruments).

3.3. Catalytic Activity for CO Methanation

The catalytic activities of the prepared MoS_2 catalysts were examined for the methanation of CO (Equation (1)).

$$H_2 + CO \rightarrow {}^{1}\!/_{2}CH_4 + {}^{1}\!/_{2}CO_2 \tag{1}$$
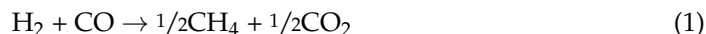
The catalytic reaction was performed in a fixed-bed reactor equipped with two K-type thermocouples to monitor the temperatures at the top and bottom of the catalyst bed. The catalyst (0.5 g) was mounted in the reactor, which was then purged with Ar gas (80 mL/min) for 30 min. The methanation reaction was performed at 400 °C under a pressure of 3 MPa using a reactant gas mixture composed of H_2 (50 vol.%) and CO (50 vol.%) (i.e., a H_2/CO ratio of 1.0). The flow rate of the reactant gas mixture was 80 mL/min, corresponding to a gas hourly space velocity (GHSV) of 4800 h^{-1}. The composition of the gaseous reaction products was analyzed using an HP 6890 Series II gas chromatograph equipped with a packed column (Carbosphere®) and a thermal conductivity detector. As a measure of the catalytic activity of MoS_2, the CO conversion

was calculated using Equation (2) under the assumption that the mass balance is satisfied by 100%.

$$\text{CO conversion (\%)} = \left(\sum n_i V_i / V_{CO}\right) \times 100 \tag{2}$$

where n_i is the number of carbon atoms in product i, V_i is the volume fraction of product i, and V_{CO} is the volume fraction of carbon monoxide in the reactant gas.

4. Conclusions

MoS_2 was synthesized from ATTM as a precursor using a high-pressure hydrothermal method at various pH values. The MoS_2 sample prepared at pH 4.5 consisted of aggregates of irregular particles. However, increasing the pH from 4.5 to 9.5 resulted in the formation of flower-like MoS_2 particles through the agglomeration of fine nanoflakes with mesopores. Based on the XRD and TEM results, hydrothermal synthesis at a pH of 9.5 could improve the crystallinity of MoS_2 by enhancing the stacking of the (0 0 2) lattice planes and increasing their lateral length. The XPS spectra confirmed that the surface Mo and S species mostly existed as Mo^{4+} and S^{2-} in the form of MoS_2. However, the sample prepared at pH 4.5 contained a large amount of Mo^{5+} in the form of Mo_2S_5 and fewer sulfate species, which led to very low CO conversion during the methanation reaction. By contrast, the high CO conversion over the samples prepared at pH 7.0 and 9.5 exhibited a low concentration of Mo^{5+} species and the presence of sulfate species that might have created sulfur vacancies that facilitated methanation. Therefore, it was concluded that using the precursor solution with pH 9.5 for hydrothermal synthesis could promote the development of MoS_2 with a flower-like morphology and the decomposition of ATTM to generate active sites for CO methanation.

Author Contributions: Conceptualization, S.-S.K.; data curation, S.-J.L. and S.-Y.P.; funding acquisition, S.-J.L.; investigation, Y.-S.S.; methodology, Y.-S.S.; project administration, S.-J.L.; resources, Y.-S.S.; supervision, J.-H.C. and S.-Y.P.; validation, J.-H.C., S.-S.K. and S.-Y.P.; visualization, S.-J.L.; writing—original draft, Y.-S.S.; writing—review and editing, S.-J.L. All authors have read and agreed to the published version of the manuscript.

Institutional Review Board Statement: Not applicable.

Informed Consent Statement: Not applicable.

Data Availability Statement: Not applicable.

Conflicts of Interest: The authors declare no conflict of interest.

References

1. Wang, Q.; Kalantar-Zadeh, K.; Kis, A.; Coleman, J.N.; Strano, M.S. Electronics and optoelectronics of two-dimensional transition metal dichalcogenides. *Nat. Nanotechnol.* **2012**, *7*, 699–712. [CrossRef]
2. Gupta, D.; Chauhan, V.; Kumar, R. A comprehensive review on synthesis and applications of molybdenum disulfide (MoS_2) material: Past and recent developments. *Inorg. Chem. Commun.* **2020**, *121*, 108200. [CrossRef]
3. Krishnan, U.; Kaur, M.; Singh, K.; Kumar, M.; Kumar, A. A synoptic review of MoS_2: Synthesis to applications. *Superlattice Microst.* **2019**, *128*, 274–297. [CrossRef]
4. Tye, C.T.; Smith, K.J. Catalytic activity of exfoliated MoS_2 in hydrodesulfurization, hydrodenitrogenation and hydrogenation reactions. *Top. Catal.* **2006**, *37*, 129–135. [CrossRef]
5. Rivera-Muñoz, E.; Lardizabal, D.; Alonso, G.; Aguilar, A.; Siadati, M.H.; Chianelli, R.R. Silica Gel- and MCM-41-supported MoS_2 catalysts for HDS reactions. *Catal. Lett.* **2003**, *85*, 147–151. [CrossRef]
6. Jian, M.; Prins, R. The effect of phosphorus on the HDN reaction of piperidine, decahydroquinoline and ortho-propylaniline over Ni-MoS_2/Al_2O_3 catalysts. *Catal. Lett.* **1995**, *35*, 193–203. [CrossRef]

7. Lee, J.S.; Kim, S.; Lee, K.H.; Nam, I.-S.; Chung, J.S.; Kim, Y.G.; Woo, H.C. Role of alkali promoters in K/MoS$_2$ catalysts for CO-H$_2$ reactions. *Appl. Catal. A* **1994**, *110*, 11–25. [CrossRef]
8. Youchang, X.; Naasz, B.N.; Somorjai, G.A. Alcohol synthesis from Co and H$_2$ over molybdenum sulfide. The effect of pressure and promotion by potassium carbonate. *Appl. Catal. A* **1986**, *27*, 233–241. [CrossRef]
9. Chen, J.; Kuriyama, N.; Yuan, H.; Takeshita, H.T.; Sakai, T. Electrochemical hydrogen storage in MoS$_2$ nanotubes. *J. Am. Chem. Soc.* **2001**, *123*, 11813–11814. [CrossRef]
10. Li, X.-L.; Li, Y.-D. MoS$_2$ nanostructures: synthesis and electrochemical Mg^{2+} intercalation. *J. Phys. Chem. B* **2004**, *108*, 13893–13900. [CrossRef]
11. Wang, Q.; Li, J. Facilitated lithium storage in MoS$_2$ overlayers supported on coaxial carbon nanotubes. *J. Phys. Chem. C* **2007**, *111*, 1675–1682. [CrossRef]
12. Du, G.; Guo, Z.; Wang, S.; Zeng, R.; Chen, Z.; Liu, H. Superior stability and high capacity of restacked molybdenum disulfide as anode material for lithium ion batteries. *Chem. Commun.* **2010**, *46*, 1106–1108. [CrossRef]
13. Rapoport, L.; Bilik, Y.; Feldman, Y.; Homyonfer, M.; Cohen, S.R.; Tenne, R. Hollow nanoparticles of WS$_2$ as potential solid-state lubricants. *Nature* **1997**, *387*, 791–793. [CrossRef]
14. Chen, W.X.; Tu, J.P.; Xu, Z.D.; Tenne, R.; Rosenstveig, R.; Chen, W.L.; Gan, H.Y. Wear and friction of Ni-P electroless composite coating including inorganic fullerene-WS$_2$ nanoparticles. *Adv. Eng. Mater.* **2002**, *4*, 686–690. [CrossRef]
15. David, L.; Bhandavat, R.; Singh, G. MoS$_2$/graphene composite paper for sodium-ion battery electrodes. *ACS Nano* **2014**, *8*, 1759–1770. [CrossRef]
16. Yang, F.; Feng, X.; Glans, P.-A.; Guo, J. MoS$_2$ for beyond lithium-ion batteries. *APL Mater.* **2021**, *9*, 050903. [CrossRef]
17. Nawz, T.; Safdar, A.; Hussain, M.; Lee, D.S.; Siyar, M. Graphene to Advanced MoS$_2$: A Review of structure, synthesis, and optoelectronic device application. *Crystals* **2020**, *10*, 902. [CrossRef]
18. Samy, O.; Zeng, S.; Birowosuto, M.D.; Moutaouakil, A.E. A Review on MoS$_2$ properties, synthesis, sensing applications and challenges. *Crystals* **2021**, *11*, 355. [CrossRef]
19. Zhang, C.; Wu, H.B.; Guo, Z.; Lou, X.W. Facile synthesis of carbon-coated MoS$_2$ nanorods with enhanced lithium storage properties. *Electrochem. Commun.* **2012**, *20*, 7–10. [CrossRef]
20. Remskar, M.; Mrzel, A.; Virsek, M.; Godec, M.; Krause, M.; Kolitsch, A.; Singh, A.; Seabaugh, A. The MoS$_2$ nanotubes with defect-controlled electric properties. *Nanoscale Res. Lett.* **2011**, *6*, 26. [CrossRef]
21. Li, Y.B.; Bando, Y.; Golberg, D. MoS$_2$ nanoflowers and their field-emission properties. *Appl. Phys. Lett.* **2003**, *82*, 1962–1964. [CrossRef]
22. Wiesel, I.; Popovitz-Biro, R.; Tenne, R. Encapsulation of Mo$_2$C in MoS$_2$ inorganic fullerene-like nanoparticles and nanotubes. *Nanoscale* **2013**, *5*, 1499–1502. [CrossRef]
23. Ramos, M.A.; Correa, V.; Torres, B.; Flores, S.; Farias Mancilla, J.R.; Chianelli, R.R. Spherical MoS$_2$ micro particles and their surface dispersion due to addition of cobalt promoters. *Rev. Mex. Fis.* **2011**, *57*, 220–223.
24. Tian, Y.; Zhao, X.; Shen, L.; Meng, F.; Tang, L.; Deng, Y.; Wang, Z. Synthesis of amorphous MoS$_2$ nanospheres by hydrothermal reaction. *Mater. Lett.* **2006**, *60*, 527–529. [CrossRef]
25. Cheon, J.; Gozum, J.E.; Girolami, G.S. Chemical vapor deposition of MoS$_2$ and TiS$_2$ films from the metal−organic precursors Mo(S-t-Bu)$_4$ and Ti(S-t-Bu)$_4$. *Chem. Mater.* **1997**, *9*, 1847–1853. [CrossRef]
26. Li, Q.; Newberg, J.T.; Walter, E.C.; Hemminger, J.C.; Penner, R.M. Polycrystalline molybdenum disulfide (2H−MoS$_2$) nano- and microribbons by electrochemical/chemical synthesis. *Nano Lett.* **2004**, *4*, 277–281. [CrossRef]
27. Ma, L.; Xu, L.-M.; Xu, X.-Y.; Luo, Y.-L.; Chen, W.-X. Synthesis and characterization of flower-like MoS$_2$ microspheres by a facile hydrothermal route. *Mater. Lett.* **2009**, *63*, 2022–2024. [CrossRef]
28. Wei, R.; Yang, H.; Du, K.; Fu, W.; Tian, Y.; Yu, Q.; Liu, S.; Li, M.; Zou, G. A facile method to prepare MoS$_2$ with nanoflower-like morphology. *Mater. Chem. Phys.* **2008**, *108*, 188–191. [CrossRef]
29. Ma, L.; Chen, W.-X.; Li, H.; Zheng, Y.-F.; Xu, Z.-D. Ionic liquid-assisted hydrothermal synthesis of MoS$_2$ microspheres. *Mater. Lett.* **2008**, *62*, 797–799. [CrossRef]
30. Ma, L.; Chen, W.-X.; Li, H.; Xu, Z.-D. Synthesis and characterization of MoS$_2$ nanostructures with different morphologies via an ionic liquid-assisted hydrothermal route. *Mater. Chem. Phys.* **2009**, *116*, 400–405. [CrossRef]
31. Xiong, Q.Q.; Ji, Z.G. Controllable growth of MoS$_2$/C flower-like microspheres with enhanced electrochemical performance for lithium ion batteries. *J. Alloys Compd.* **2016**, *673*, 215–219. [CrossRef]
32. Liu, J.; Wang, E.; Lv, J.; Li, Z.; Wang, B.; Ma, X.; Qin, S.; Sun, Q. Investigation of sulfur-resistant, highly active unsupported MoS$_2$ catalysts for synthetic natural gas production from CO methanation. *Fuel Process. Technol.* **2013**, *110*, 249–257. [CrossRef]
33. Alonso, G.; Berhault, G.; Aguilar, A.; Collins, V.; Ornelas, C.; Fuentes, S.; Chianelli, R.R. Characterization and HDS activity of mesoporous MoS$_2$ catalysts prepared by in situ activation of tetraalkylammonium thiomolybdates. *J. Catal.* **2002**, *208*, 359–369. [CrossRef]
34. Alonso, G.; Del Valle, M.; Cruz, J.; Petranovskii, V.; Licea-Claverie, A.; Fuentes, S. Preparation of MoS$_2$ catalysts by in situ decomposition of tetraalkylammonium thiomolybdates. *Catal. Today* **1998**, *43*, 117–122. [CrossRef]
35. Choi, J.-M.; Kim, S.-H.; Lee, S.-J.; Kim, S.-S. Effects of pressure and temperature in hydrothermal preparation of MoS$_2$ catalyst for methanation reaction. *Catal. Lett.* **2018**, *148*, 1803–1814. [CrossRef]

36. Sen, U.K.; Mitra, S. High-rate and high-energy-density lithium-ion battery anode containing 2D MoS$_2$ nanowall and cellulose binder. *ACS Appl. Mater. Interfaces* **2013**, *5*, 1240–1247. [CrossRef]

37. Poh, C.K.; Onga, S.W.D.; Du, Y.H.; Kamata, H.; Choong, K.S.C.; Chang, J.; Izumi, Y.; Nariai, K.; Mizukami, N.; Chen, L.; et al. Direct methanation with supported MoS$_2$ nano-flakes: Relationship between structure and activity. *Catal. Today* **2020**, *342*, 21–31. [CrossRef]

38. Zhang, J.; Wang, Y.; Lin, Z.; Huang, F. Formation and self-assembly of cadmium hydroxide nanoplates in molten composite-hydroxide solution. *Cryst. Growth Des.* **2010**, *10*, 4285–4291. [CrossRef]

39. Ge, L.; Han, C.; Xiao, X.; Guo, L. Synthesis and characterization of composite visible light active photocatalysts MoS$_2$–g-C$_3$N$_4$ with enhanced hydrogen evolution activity. *Int. J. Hydrogen Energy* **2013**, *38*, 6960–6969. [CrossRef]

40. Chianelli, R.R.; Prestridge, E.B.; Pecoraro, T.A.; Deneufville, J.P. Molybdenum Disulfide in the poorly crystalline "rag" structure. *Science* **1979**, *203*, 1105–1107. [CrossRef]

41. Liang, K.S.; Chianelli, R.R.; Chien, F.Z.; Moss, S.C. Structure of poorly crystalline MoS$_2$-A modeling study. *J. Non-Cryst. Solids* **1986**, *79*, 251–273. [CrossRef]

42. Daage, M.; Chianelli, R.R. Structure-function relations in molybdenum sulfide catalysts: The "rim-edge" model. *J. Catal.* **1994**, *149*, 414–427. [CrossRef]

43. Sing, K.S.W.; Everett, D.H.; Haul, R.A.W.; Moscou, L.; Pierotti, R.A.; Rouquérol, J.; Siemieniewska, T. Reporting physisorption data for gas/solid systems with special reference to the determination of surface area and porosity. *Pure Appl. Chem.* **1985**, *57*, 603–619. [CrossRef]

44. Wang, H.W.; Skeldon, P.; Thompson, G.E. XPS studies of MoS$_2$ formation from ammonium tetrathiomolybdate solutions. *Surf. Coat. Technol.* **1997**, *91*, 200–207. [CrossRef]

45. Wang, H.W.; Skeldon, P.; Thompson, G.E. Thermogravimetric—Differential thermal analysis of the solid-state decomposition of ammonium tetrathiomolybdate during heating in argon. *J. Mater. Sci.* **1998**, *33*, 3079–3083. [CrossRef]

46. Topsøe, H.; Clausen, B.S.; Massoth, F.E. Hydrotreating Catalysis. In *Catalysis. Catalysis–Science and Technology*; Anderson, J.R., Boudart, M., Eds.; Springer: Berlin/Heidelberg, Germany, 1996; Volume 11, pp. 1–269. [CrossRef]

47. Byskov, L.S.; Nørskov, J.K.; Clausen, B.S.; Topsøe, H. DFT Calculations of unpromoted and promoted MoS$_2$-based hydrodesulfurization catalysts. *J. Catal.* **1999**, *187*, 109–122. [CrossRef]

48. Afanasiev, P. On the interpretation of temperature programmed reduction patterns of transition metals sulphides. *Appl. Catal. A* **2006**, *303*, 110–115. [CrossRef]

49. Li, X.S.; Xin, Q.; Guo, X.X.; Grange, P.; Delmon, B. Reversible hydrogen adsorption on MoS$_2$ studied by Temperature-programmed desorption and Temperature-programmed reduction. *J. Catal.* **1992**, *137*, 385–393. [CrossRef]

50. Iwata, Y.; Sato, K.; Yoneda, T.; Miki, Y.; Sugimoto, Y.; Nishijima, A.; Shimada, H. Catalytic functionality of unsupported molybdenum sulfide catalysts prepared with different methods. *Catal. Today* **1998**, *45*, 353–359. [CrossRef]

51. Iwata, Y.; Araki, Y.; Honna, K.; Miki, Y.; Sato, K.; Shimada, H. Hydrogenation active sites of unsupported molybdenum sulfide catalysts for hydroprocessing heavy oils. *Catal. Today* **2001**, *65*, 335–341. [CrossRef]